TASK QUARTERLY 4 No 1 (2000), 49–80

SELFEXCITED VIBRATION OF A PALISADE IN 2D SUBSONIC, TRANSONIC AND SUPERSONIC FLOW

ROMUALD RZĄDKOWSKI[1] AND ALEXANDER KOVALYOV[2]

[1]*Institute of Fluid–Flow Machinery, Polish Academy of Sciences, Fiszera 14, 80–952 Gdansk, Poland and Polish Naval Academy, Faculty of Mechanical and Electrical Engineering, Gdynia, Poland*
z3@imp.pg.gda.pl

[2]*Department of Hydromechanics of Power Machines, Institute for Problems in Machinery, Ukrainian National Academy of Sciences Pozarsky St. 2/10 Kharkov, 310046, Ukraine*

(Received 6 January 2000)

Abstract: In recent years the works of the coupled fluid–structure problems appeared. The computational method used to solve this problem was based on a time–marching algorithm, so it was natural to consider a time domain flutter analysis method. The time domain method of flutter analysis is based on the simultaneous integration in time of the equation of motion for the structure and the fluid. The flow model is capable of representing 2D–flows over a wide Mach number range from low subsonic to supersonic, including transonic flows. The aerodynamic model fully accounts for blade thickness and camber and the angle–of–attack effects. The unsteady Euler equations are integrated by using the explicit monotonous second–order accurate Godunov's scheme. The blade is modelled on a basis of extended beam theory including a bending–bending–torsional vibration and also by the simple two–degree of freedom model. The equation of motion is obtained by using the extended Hamilton's principle and the Ritz method. The direct integration method is used to find a solution of the coupled fluid–structure problem. In this work the comparison of the numerical and experimental results is presented for the First and Fourth Standard Configurations.

Keywords: blades, flutter, vibrations

1. Introduction

The traditional approach in flutter calculations of cascade has been to apply frequency domain analysis. In this approach, the blade motions are assumed to be harmonic functions of time with a constant phase lag between adjacent blades. The equations of motion then are reduced to an eigenvalue problem; the eigenvalues determine stability. This analysis is restricted to linear structural equations and aerodynamic forces that are linearly dependent on the displacements. The unsteady

aerodynamic forces used in such an analysis are typically based on classical linearized potential theory, but allow the use of efficient semianalytical solution methods.

In recent years the works on the coupled fluid–structure problems appeared. The computational method used to solve coupled fluid–structure problem was based on a time–marching algorithm, so it was natural to consider a time domain flutter analysis method. The time domain method of flutter analysis is based on the simultaneous integration in time of the equation of motion for the structure and the fluid (Bakhale *et al.* [3]). The time domain method is not restricted to linear structural models and does not require the assumption of linear relations between aerodynamic loads and blade displacements. The time domain approach allows an accurate representation of the onset of flutter in the cascades when the blades have complex shape.

He [12, 13] used 2D Navier–Stokes equations, discretized spatially by using the cell–vertex finite volume scheme. The fluid–structure equations were solved in time using the multistage Runge–Kutta scheme. The motion of each blade is governed by a structural dynamic model with two degrees of freedom, so the influence of the disc was not taken into consideration.

In this work the simultaneous time domain method is used to determine the aeroelastic stability of a bladed disc. The unsteady equations of motion for the structure and the fluid are integrated simultaneously in time starting with a steady flowfiel and a small initial disturbances applied to the airfoil. Each blade is allowed to move independently, and the motion of all blades is analyzed to determine the aeroelastic stability of the bladed disc. The flow model is capable of representing 2D–flows over a wide Mach number range from low subsonic to supersonic, including transonic flows. The aerodynamic model fully accounts for blade thickness and camber and the angle–of–attack effects. The unsteady Euler equations are integrated by using the explicit monotonous second–order accurate Godunov's scheme. The blade is modelled on a basis of extended beam theory including a bending–bending–torsional vibration and also by the simple two–degree of freedom model. The equation of motion is obtained by using the extended Hamilton's principle and the Ritz method. The direct integration method is used to find a solution of the coupled fluid–structure problem.

2. The structure models

Two structure models were presented. In the first one the blade is modelled by the continuous model. In the second one the blades are modelled by the two–degree of freedom model.

2.1 The continuous model

The blade model applied here is a one–dimensional beam described by an extended beam–theory including all important effects on a rotating blade. The model was described in detail in the reference (see Rządkowski [18]). The disc is modelled by a moderately thick plate theory. Assuming rigidly fixed blades on the disk rim, the

displacements of any particle of the bladed disc are written in the form:

$$\mathbf{u} = \mathbf{U}\mathbf{q}, \tag{1}$$

where

$$\mathbf{u} = col(\mathbf{u}_1, \ldots, \mathbf{u}_N, \mathbf{u}_d),$$

$$\mathbf{q} = col(\mathbf{q}_1, \ldots, \mathbf{q}_N, \mathbf{q}_d),$$

$$\mathbf{U} = \begin{bmatrix} \mathbf{U}_1 & \mathbf{0} & \ldots & \mathbf{0} & \mathbf{U}_{sp1} \\ \mathbf{0} & \mathbf{U}_2 & \ldots & \mathbf{0} & \mathbf{U}_{sp2} \\ . & . & . & . & . \\ \mathbf{0} & \mathbf{0} & \ldots & \mathbf{U}_N & \mathbf{U}_{spN} \\ \mathbf{U}_{sp1}^T & \mathbf{U}_{sp2}^T & \ldots & \mathbf{U}_{spN}^T & \mathbf{U}_d \end{bmatrix},$$

$\mathbf{u}_i$ is the vector of generalized displacements of each point of the i–th blade, $\mathbf{u}_d$ is the vector of generalized displacements of each point of the disc, $\mathbf{q}_i$ are the unknown functions of the ith blade and the $\mathbf{q}_d$ are the unknown functions of the disc, both describing the displacement field. The matrices $\mathbf{u}$, $\mathbf{q}$, $\mathbf{U}_i$, $\mathbf{U}_d$, $\mathbf{U}_{spi}$, $i = 1, \ldots, N$ are shown in (Rządkowski [18–20]).

The blades and disc material are modeled as a Hooke's material.

In order to find an approximate solution of the forced vibrations of the mistuned bladed disc, the Hamilton principle can be used:

$$\delta \int_{t_1}^{t_2} (\mathcal{E} - \mathcal{K})\, \mathrm{d}t = \int_{t_1}^{t_2} \delta(\mathcal{W} - \mathcal{D})\, \mathrm{d}t, \tag{2}$$

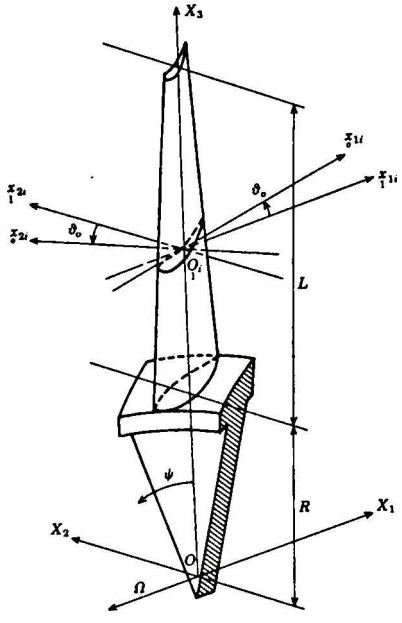

***Figure 1.** Model of the bladed disc*

where $\mathcal{E}$ and $\mathcal{K}$ are elastic and kinetic energies, respectively, given by:

$$\mathcal{E} = 0.5\int_B \mathbf{C}_e \cdot (\mathbf{E} \otimes \mathbf{E}) \mathrm{d}V, \quad \mathcal{K} = 0.5\int_B \rho \dot{\mathbf{u}} \dot{\mathbf{u}} \mathrm{d}V, \tag{3}$$

where $\mathbf{C}_e$ and $\mathbf{E}$ are the tensors of elastic coefficients and the Green deformation, respectively, and $\delta \mathcal{W}$ and $\delta \mathcal{D}$ are the variations of external work and the internal dissipative forces, respectively.

Following the above equations, the equation of motion of the bladed disc for the forced vibration is represented by the equation:

$$\mathbf{M}\ddot{\mathbf{y}} + \mathbf{C}\dot{\mathbf{y}} + \mathbf{K}\mathbf{y} = \mathbf{F}, \tag{4}$$

where **M**, **C** (see [19], p. 91), **K** are the mass, damping and stiffness matrix of the bladed disc, respectively, **y** unknown vector (see [19], p. 38) and **F** is the vector of external forces (will be taken from the flow program in time step procedure (see [19], p. 91)).

The aeroelastic equation (see equation (4)):

$$\mathbf{M}\ddot{\mathbf{y}}_{t_m} + \mathbf{C}\dot{\mathbf{y}}_{t_m} + \mathbf{K}\mathbf{y}_{t_m} = \mathbf{F}_{t_m} \tag{5}$$

is integrated at a considered point of time $t_m = t_o + m\Delta t$, by a method of constant average acceleration.

For each point of time t_m, the excitation generalized forces $\mathbf{F}_{t_m}$ must be calculated from the flow model, for the position of the blades in cascade, calculated by the structure model.

To obtain the solution for the general displacements at time $t + \Delta t$, the equilibrium conditions (see equation (4)) are considered at time $t + \theta\Delta t$. However, be-cause the acceleration is assumed to vary linearly, a linearly projected load vector is used; i.e., the equation employed is:

$$\mathbf{M}\ddot{\mathbf{y}}_{t+\theta\Delta t} + \mathbf{C}\dot{\mathbf{y}}_{t+\theta\Delta t} + \mathbf{K}\mathbf{y}_{t+\theta\Delta t} = \mathbf{F}_{t+\theta\Delta t}, \tag{6}$$

where

$$\mathbf{F}_{t+\Delta t} = \mathbf{F}_t + \theta(\mathbf{F}_{t+\Delta t} - \mathbf{F}_t). \tag{7}$$

The Wilson θ method, in which a linear variation of acceleration from time t to time $t + \Delta t$ is assumed. For the unconditional stability we employ $\theta = 1.4$.

Let τ denote the increase in time, where $0 < \tau < \theta\Delta t$; then for the time interval t to $t + \theta\Delta t$, it is assumed that:

$$\ddot{\mathbf{y}}_{t+\tau} = \ddot{\mathbf{y}}_t + (\tau / \theta\Delta t)(\ddot{\mathbf{y}}_{t+\theta\Delta t} - \ddot{\mathbf{y}}_t). \tag{8}$$

Integrating equation (8), we obtain:

$$\dot{\mathbf{y}}_{t+\tau} = \dot{\mathbf{y}}_t + \ddot{\mathbf{y}}_t\tau + (\tau^2 / 2\theta\Delta t)(\dot{\mathbf{y}}_{t+\theta\Delta t} - \dot{\mathbf{y}}_t), \tag{9}$$

and

$$\mathbf{y}_{t+\tau} = \mathbf{y}_t + \dot{\mathbf{y}}_t\tau + 0.5\ddot{\mathbf{y}}_t\tau^2 + (\tau^3 / 6\theta\Delta t)(\ddot{\mathbf{y}}_{t+\theta\Delta t} - \ddot{\mathbf{y}}_t). \tag{10}$$

Using (9) and (10), we have at time $t + \theta\Delta t$:

$$\dot{\mathbf{y}}_{t+\theta\Delta t} = \dot{\mathbf{y}}_t + (\theta\Delta t/2)(\ddot{\mathbf{y}}_{t+\theta\Delta t} + \ddot{\mathbf{y}}_t), \tag{11}$$

$$\mathbf{y}_{t+\theta\Delta t} = \mathbf{y}_t + \theta\Delta t\dot{\mathbf{y}}_t + (\theta^2\Delta t^2/6)(\ddot{\mathbf{y}}_{t+\theta\Delta t} + 2\ddot{\mathbf{y}}_t), \tag{12}$$

from which we can solve for $\ddot{\mathbf{y}}_{t+\theta\Delta t}$ and $\dot{\mathbf{y}}_{t+\theta\Delta t}$ in terms of $\mathbf{y}_{t+\theta\Delta t}$:

$$\ddot{\mathbf{y}}_{t+\theta\Delta t} = \frac{6}{\theta^2\Delta t^2}(\mathbf{y}_{t+\theta\Delta t} - \mathbf{y}_t) + \frac{6}{\theta\Delta t}\dot{\mathbf{y}}_t - 2\ddot{\mathbf{y}}_t, \tag{13}$$

and

$$\dot{\mathbf{y}}_{t+\theta\Delta t} = \frac{3}{\theta\Delta t}(\mathbf{y}_{t+\theta\Delta t} - \mathbf{y}_t) - 2\dot{\mathbf{y}}_t - \frac{\theta\Delta t}{2}\ddot{\mathbf{y}}_t. \tag{14}$$

2.2 The discrete model

The equation of motion of the bladed disc for the forced vibration can be expressed by equation (4). The general displacement vector **y** is transformed in mode shape space by using the transformation (see [4], pp. 326–343):

$$\mathbf{y}(t) = \sum_{k=1}^{K} \mathbf{P}_k x_k(t) = \mathbf{P}\mathbf{x}, \tag{15}$$

where $x_k(t)$ are the time–dependent modal co–ordinates of the problems, and $\mathbf{P}_k$ denotes the k–th mode shape vector (see [19], p. 38).

Introducing equation (15) into equation (4) and using ([4], p. 328):

$$\mathbf{P}^T\mathbf{M}\mathbf{P} = \mathbf{I}, \qquad \mathbf{P}^T\mathbf{K}\mathbf{P} = \boldsymbol{\Omega}^2, \tag{16}$$

where the **P** matrix columns are the eigenvectors $\mathbf{P}_k$ and $\boldsymbol{\Omega}^2$ is a diagonal matrix which stores the eigenvalues ω_k^2 (see [19], p. 38), one obtains the equilibrium equation that corresponds to the modal generalized displacements:

$$\ddot{\mathbf{x}} + \mathbf{P}^T\mathbf{C}\mathbf{P}\dot{\mathbf{x}} + \boldsymbol{\Omega}^2\mathbf{x} = \mathbf{P}^T\mathbf{F}. \tag{17}$$

The initial conditions for **x** are obtained by using equations (15) and (16): i.e., at time $t = 0$ one has:

$$\mathbf{x}_0 = \mathbf{P}^T\mathbf{M}\mathbf{y}_0, \qquad \dot{\mathbf{x}}_0 = \mathbf{P}^T\mathbf{M}\dot{\mathbf{y}}_0. \tag{18}$$

Let (see [4], p. 338):

$$\mathbf{P}_k^T\mathbf{C}\mathbf{P}_j = 2\omega_k\xi_k\delta_{kj}, \tag{19}$$

where ξ_k is a modal damping parameter, δ_{kj} is the Kroneker delta and ω_k is an angular natural frequency of bladed disc. Then, using equation (19) reduces equation (17) to n equations of the form:

$$\ddot{x}_k + 2\omega_k\xi_k\dot{x}_k + \omega_k^2 x_k = r_k, \tag{20}$$

where $r_k = \mathbf{P}_k^T\mathbf{F}$ and the initial conditions for x_k have already been defined in equation (18).

For a constant force $\mathbf{F}_0$ acting during a period Δt one obtains the linear differential equation of second order with constant coefficients (see [16], p. 163):

$$\ddot{x}_k + 2\omega_k \xi_k \dot{x}_k + \omega_k^2 x_k = r_k. \tag{21}$$

The solution of equation (21) is known in the form (see [1], p. 153–156):

$$x_k = e^{(-\xi_k \omega_k \Delta t)}(C_2 \sin \overline{\omega}_k \Delta t + C_1 \cos \overline{\omega}_k \Delta t) + \frac{r_k}{\omega_k^2}, \qquad t \in (t_1, t_1 + \Delta t), \tag{22}$$

where

$$\overline{\omega}_k = \omega_k \sqrt{1 - \xi_k^2}, \qquad C_1(t_1) = x_0(t_1) - \frac{r_k(t_1)}{\omega_k(t_1)^2}, \tag{23}$$

and

$$C_2(t_1) = (\dot{x}_0(t_1) + \omega_k \xi_k (x_0(t_1) - \frac{r_k(t_1)}{\omega_k(t_1)^2})) \frac{1}{\overline{\omega}_k},$$

in which x_0(t) and $\dot{x}_0(t)$ are the modal displacement and velocity at the beginning of the period Δt.

This is a very general model. Let assume that the blades are non–twisted with a constant cross–sectional area along the blade length. The centre of shear and gravity of the blade cross–sections coincide. Let us consider the motion of n–th blade as plane motion of the solid body with two degrees of freedom. The transverse displacements in x, y directions h_{x_n}, h_{y_n}:

$$h_{x_n}(t) = h_{x_0} \sin[\omega t + (n-1)\delta];$$
$$h_{y_n}(t) = h_{y_0} \sin[\omega t + (n-1)\delta];$$

$\alpha_y(t)$ defines the torsion oscillations of the n–th blade:

$$\alpha_n(t) = \alpha_0 \sin[\omega t + (n-1)\delta]. \tag{24}$$

Here h_{x_0}, h_{y_0}, α_0 are the amplitudes of oscillations the same for all blades; ω is oscillation angular frequency; δ is the constant interblade phase angle; n is the blade number.

The equations (20) are reduced to set of three ordinary linear differential equations of first order for only torsion (α_n) and bending (h_{x_n}, h_{y_n}). For a constant force $\mathbf{F}_0$ acting during a period Δt one obtains the linear differential equations of second order with the constant coefficients:

$$\ddot{h}_k + 2\omega_k \xi_k \dot{h}_k + \omega_k^2 h_k = r_k, \qquad k = (h_{x_n}, h_{y_n}, \alpha_n) \tag{25}$$

where ξ_k is a modal damping parameter (see [8], see p. 338), ω_k is an angular natural frequency of the blade.

3. The unsteady aerodynamic model

Let us consider the transonic flow of an ideal gas through a plane multipassage cascade. In a general case the flow is assumed to be periodic from blade to blade (in pitchwise direction), so the calculated domain includes all profiles of an annular cascade (see Figure 2).

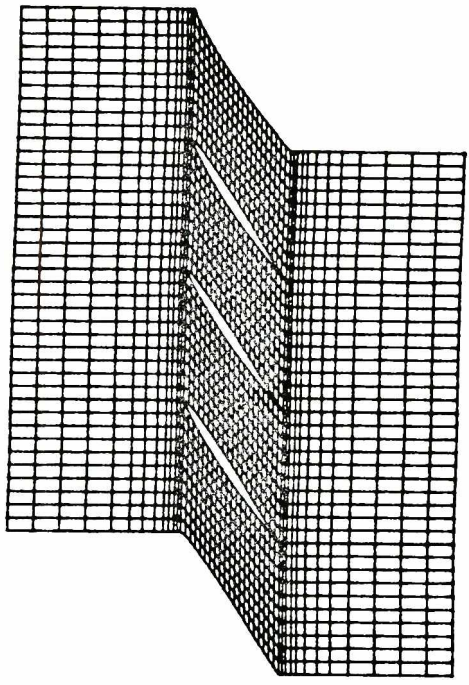

Figure 2. *Calculation domain*

The 2D unsteady transonic flow of the ideal gas is described by Euler equations, represented as the conservation laws in the Cartesian coordinate system:

$$\frac{\partial}{\partial t}\mathbf{U}+\frac{\partial}{\partial x}\mathbf{F}_1+\frac{\partial}{\partial y}\mathbf{F}_2=0, \tag{26}$$

where

$$\mathbf{U}=\begin{bmatrix}\rho\\ \rho v_1\\ \rho v_2\\ E\end{bmatrix},\quad \mathbf{F}_1=\begin{bmatrix}\rho v_1\\ p+\rho v_1^2\\ \rho v_1 v_2\\ (p+e)v_1\end{bmatrix},\quad \mathbf{F}_2=\begin{bmatrix}\rho v_2\\ \rho v_1 v_2\\ p+\rho v_2^2\\ (p+e)v_2\end{bmatrix}.$$

Here p, ρ are the pressure and density; v_1, v_2 are the velocity components in x and y directions; $e = \rho(\varepsilon + (v_1^2 + v_2^2)/2)$ is the full energy of volume unit; ε is an internal energy of mass unit, which is defined from the state equation of a perfect gas:

$$\varepsilon=\frac{1}{\kappa-1}\frac{p}{\rho},$$

κ is the ratio of specific heats.

The differential equation (26) is integrated on moving H–type grid with the use of the explicit monotonous second–order accuracy Godunov's type difference scheme.

The general algorithm of the problem was the principle of relaxation over time, as a transition from the state in time moment equal to t_0 to the state in time moment equal to $t_0 + \tau$. Let us obtain the calculated formulas for this transition on an arbitrary moving grid by Godunov's idea [11], but in a more universal form.

Let the problem be characterized by the set of parameters at moment t_0 in the grid cells, which cover all the domain:

$$\{p, \rho, v_1, v_2\}_{i+\frac{1}{2}, j+\frac{1}{2}} \quad (i = 1, \ldots, M; j = 1, \ldots, N),$$

where M is the number of cells in the y direction and N is the number of cells in the x direction. The same values at moment $t_0 + \tau$ are denoted by:

$$\{p, \rho, v_1, v_2\}^{i+\frac{1}{2}, j+\frac{1}{2}}.$$

We assume, that by use of the algorithm of H–grid generation we can obtain the coordinates and velocity components of all points, for two moments t_0 and $t_0 + \tau$.

Equations (26) can be represented as the integral conservation laws:

$$\oint_\sigma (\mathbf{U}dxdy + \mathbf{F}_1 dydt + \mathbf{F}_2 dxdt) = 0, \tag{27}$$

where the integration can be performed over any closed directed surface in the space x, y, t.

Let us apply the integrals (27) to the separate grid cell with number $\{i + 1/2, j + 1/2\}$ during time from t_0 till $t_0 + \tau$, so each grid cell is a hexahedron of the curvilinear surface, shown in Figure 3. The lower base of the hexahedron is grid cell at moment t_0, and the upper base is the grid cell at moment $t_0 + \tau$. Assuming that the velocities of points are constant during the time step τ, let us connect the points of the bases by straight line intercepts. The lateral side can be represented by the surface stretched on the frame of four line segments in space x, y, t (points of

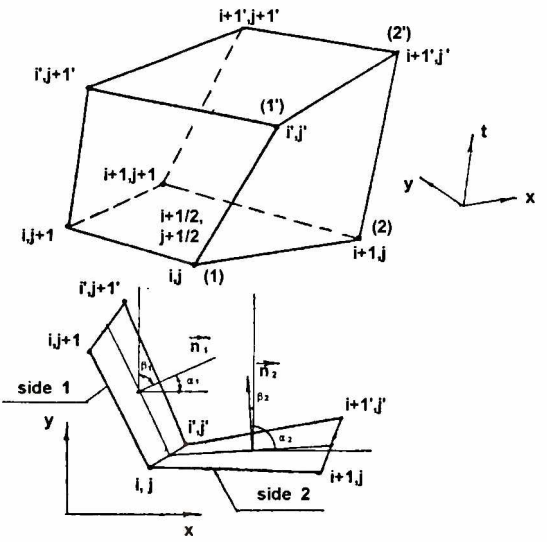

Figure 3. Cell of moving grid

the lower surface ($t = t_0$) with the upper surface ($t = t_0 + \tau$), for example side 1, 2, 1′, 2′, see Figure 3).

In order to better understand the moving grid calculations, let us concentrate from the very beginning on the not moving grid. In the not moving grid the cell is a rectangular prism, in which areas $\sigma^{i+\frac{1}{2},j+\frac{1}{2}}$ and $\sigma_{i+\frac{1}{2},j+\frac{1}{2}}$ are the same (see Figure 4). Let the distance between the points $(i, j + 1)$ and (i, j) be h_y, and between points (i,j) and $(i + 1, j)$ be h_x.

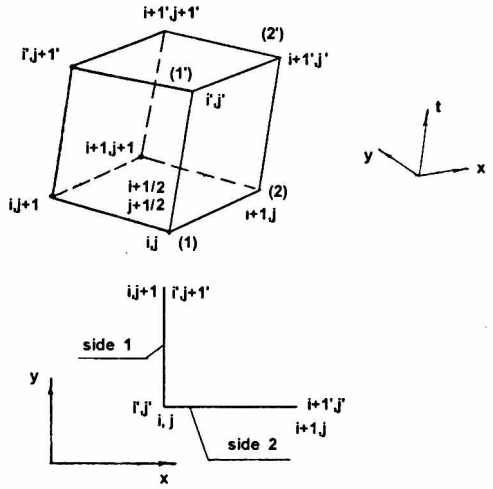

Figure 4. *Cell of not–moving grid*

Let's take into account the first equation of (27):

$$\oint (\rho dxdy + \rho v_1 dydt + \rho v_2 dxdt) = 0. \tag{28}$$

Integrating equations (28) over a rectangular prism $(i + 1/2,\ j + 1/2)$, and denoting the considered values of the upper and lower bases with half–integer indexes, and considered values of the lateral sides with integer and half–integer indexes, we shall obtain:

$$\begin{aligned} &\rho^{i+\frac{1}{2},j+\frac{1}{2}} h_x h_y - \rho_{i+\frac{1}{2},j+\frac{1}{2}} h_x h_y + \int_{t_0}^{t_0+\tau}\int_{y_j}^{y_{j+1}} \rho(v_1)_{x=x_{i+1}}\, dydt - \\ &- \int_{t_0}^{t_0+\tau}\int_{y_j}^{y_{j+1}} \rho(v_1)_{x=x_i}\, dydt + \int_{t_0}^{t_0+\tau}\int_{x_j}^{x_{j+1}} \rho(v_2)_{y=y_{j+1}}\, dxdt - \\ &- \int_{t_0}^{t_0+\tau}\int_{x_j}^{x_{j+1}} \rho(v_2)_{y=y_j}\, dxdt = 0. \end{aligned} \tag{29}$$

In these equations

$$\int_{t_0}^{t_0+\tau}\int_{y_j}^{y_{j+1}} \rho(v_1)_{x=x_{i+1}}\, dydt \tag{30}$$

means the integral on the boundary between cells $(i + 1/2, j + 1/2)$ and $(i + 3/2, j + 1/2)$. This surface will be denoted by $(i + 1, j + 1/2)$. The values of ρ, v_1, v_2 will be different for each cell, so let's denote these values on the boundary $i+1$ between cells $(i + 1/2, j + 1/2)$ and $(i + 3/2, j + 1/2)$ in the period of time $(t_0, t_0 + \tau)$, by $R_{i+1, j+1/2}$, $V_{1i+1, j+1/2}$, $V_{2i+1, j+1/2}$.

So (29) can be written in the form:

$$\rho^{i+\frac{1}{2},j+\frac{1}{2}} - \rho_{i+\frac{1}{2},j+\frac{1}{2}} + \frac{\tau}{h_x}[(RV_1)_{i+1,j+\frac{1}{2}} - (RV_1)_{i,j+\frac{1}{2}}] + \\ + \frac{\tau}{h_y}[(RV_2)_{i+\frac{1}{2},j+1} - (RV_2)_{i+\frac{1}{2},j}] = 0. \tag{31}$$

Other equations of (27) can be calculated similarly. The values R, V_1, V_2, P, E on the boundary are not known yet, the small values in the cell ρ, v_1, v_2, p, e are known (see Figures 9 and 10). In order to find these values the solution for the local Riemann problem at the cell interfaces must be found. This is the physical step of the whole procedure. The discontinuities at the interfaces are resolved in a superposition of waves satysfying locally the conservations equations. (see Godunov [11], p.105 and 130, Hirsch [15], p.443, Chmielniak [9], p. 160).

The above equations can be written in the general form:

$$\mathbf{U}^{i+\frac{1}{2},j+\frac{1}{2}}\sigma^{i+\frac{1}{2},j+\frac{1}{2}} = \mathbf{U}_{i+\frac{1}{2},j+\frac{1}{2}}\sigma_{i+\frac{1}{2},j+\frac{1}{2}} - \\ - \mathbf{Q}_{i+1,j+\frac{1}{2}} - \mathbf{Q}_{i,j+\frac{1}{2}} - \mathbf{Q}_{i+\frac{1}{2},j+1} - \mathbf{Q}_{i+\frac{1}{2},j}, \tag{32}$$

where for example $\mathbf{Q}_{i+1, j+1/2}$ can be written in the form:

$$\mathbf{Q}_{i+1,j+\frac{1}{2}} = \mathbf{F}_{1_{i+1,j+\frac{1}{2}}}\Phi_{i+1,j+\frac{1}{2}} + \mathbf{F}_{2_{i+1,j+\frac{1}{2}}}\Psi_{i+1,j+\frac{1}{2}}, \tag{33}$$

where

$$\sigma_{i+1,j+\frac{1}{2}} = \int_{i+1}\int_{j+\frac{1}{2}} dxdy, \\ \Phi_{i+1,j+\frac{1}{2}} = \int_{i+1}\int_{j+\frac{1}{2}} dydt, \\ \Psi_{i+1,j+\frac{1}{2}} = \int_{i+1}\int_{j+\frac{1}{2}} dxdt, \tag{34}$$

$$\sigma(x_1,y_1,x_2,y_2,x_3,y_3,x_4,y_4) = 0.5[(x_3 - x_1)(y_4 - y_2) - (x_4 - x_2)(y_3 - y_1)],$$

and x_1, y_1, x_2, y_2, x_3, y_3, x_4, y_4 are coordinates shown in Figure 5.

In case of moving grid the form of equation (32) is the same but, for example $\mathbf{Q}_{i+1, j+1/2}$ can be writen in the form:

$$\mathbf{Q}_{i+1,j+\frac{1}{2}} = \mathbf{U}_{i+1,j+\frac{1}{2}}\sigma_{i+1,j+\frac{1}{2}} + \mathbf{F}_{1_{i+1,j+\frac{1}{2}}}\Phi_{i+1,j+\frac{1}{2}} + \mathbf{F}_{2_{i+1,j+\frac{1}{2}}}\Psi_{i+1,j+\frac{1}{2}}, \tag{35}$$

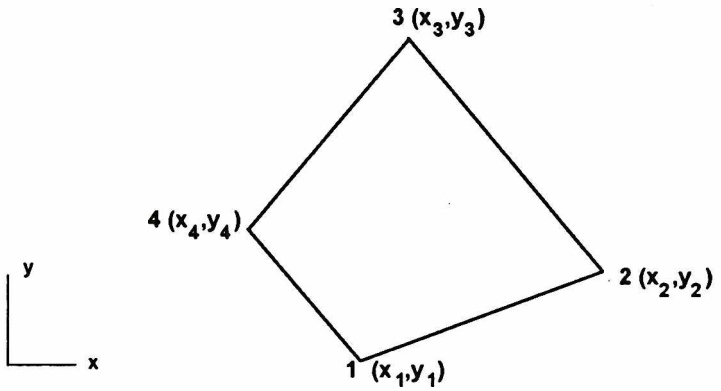

Figure 5. *The coordinates of the cell*

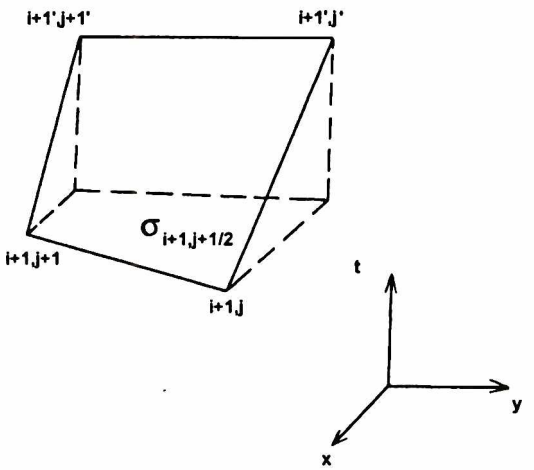

Figure 6. *The moving grid*

where $\sigma_{i+1,j+1/2}$ is the projection of the surface $((i+1,j+1)(i+1,j)(i+1',j')$ $(i+1',j+1'))$ on the plane (xy) (see Figure 6).

In order to find components of (32) in a general case, equations (27) were integrated over the surface shown in Figure 3. Denoting the considered values of the upper and lower bases with half–integer indexes, and considered values of the lateral sides with integer and half–integer indexes, we obtain:

$$\mathbf{U}^{i+\frac{1}{2},j+\frac{1}{2}}\sigma^{i+\frac{1}{2},j+\frac{1}{2}} - \mathbf{U}_{i+\frac{1}{2},j+\frac{1}{2}}\sigma_{i+\frac{1}{2},j+\frac{1}{2}} + \tag{36}$$

$$+(\mathbf{U}\sigma\cos\gamma_1)_{i+1,j+\frac{1}{2}} - (\mathbf{U}\sigma\cos\gamma_1)_{i,j+\frac{1}{2}} + (\mathbf{U}\sigma\cos\gamma_2)_{i+\frac{1}{2},j+1} - (\mathbf{U}\sigma\cos\gamma_2)_{i+\frac{1}{2},j} +$$

$$+(\mathbf{F}_1\sigma\cos\alpha_1)_{i+1,j+\frac{1}{2}} - (\mathbf{F}_1\sigma\cos\alpha_1)_{i,j+\frac{1}{2}} + (\mathbf{F}_1\sigma\cos\alpha_2)_{i+\frac{1}{2},j+1} - (\mathbf{F}_1\sigma\cos\alpha_2)_{i+\frac{1}{2},j} +$$

$$+(\mathbf{F}_2\sigma\cos\beta_1)_{i+1,j+\frac{1}{2}} - (\mathbf{F}_2\sigma\cos\beta_1)_{i,j+\frac{1}{2}} + (\mathbf{F}_2\sigma\cos\beta_2)_{i+\frac{1}{2},j+1} - (\mathbf{F}_2\sigma\cos\beta_2)_{i+\frac{1}{2},j} = 0.$$

Here σ is the area of the cell side; ($\cos\alpha_1$, $\cos\beta_1$, $\cos\gamma_1$) and ($\cos\alpha_2$, $\cos\beta_2$, $\cos\gamma_2$) are the direction cosines of normals $\mathbf{n}_1$ and $\mathbf{n}_2$ to the lateral sides (see Figure 3).

Let us introduce into consideration the mean line length Γ for every lateral side and velocity W_n of the mean line center motion in the direction to it's normal. Then the lateral sides projections on the coordinate planes ($\cos\alpha$, $\cos\beta$, $\cos\gamma$) can be represented as:

$$\begin{aligned} \sigma\cos\alpha_1 &= \Delta t\Gamma_1\cos\alpha_1; \quad \sigma\cos\alpha_2 = \Delta t\Gamma_2\cos\alpha_2; \\ \sigma\cos\beta_1 &= \Delta t\Gamma_1\cos\beta_1; \quad \sigma\cos\beta_2 = \Delta t\Gamma_2\cos\beta_2; \\ \sigma\cos\gamma_1 &= -\Delta t W_{n_1}\Gamma_1; \quad \sigma\cos\gamma_2 = -\Delta t W_{n_2}\Gamma_2. \end{aligned} \tag{37}$$

Taking into account (36) and (37) let us write the calculated formulas of gasdynamic parameters at moment $t_0 + \tau$:

$$\rho^{i+\frac{1}{2},j+\frac{1}{2}} = \frac{\sigma_{i+\frac{1}{2},j+\frac{1}{2}}}{\sigma^{i+\frac{1}{2},j+\frac{1}{2}}}\rho_{i+\frac{1}{2},j+\frac{1}{2}} -$$

$$-\frac{\tau}{\sigma^{i+\frac{1}{2},j+\frac{1}{2}}}\{[(-W_n+v_n)\rho\Gamma_1]|_{i+1} - [(-W_n+v_n)\rho\Gamma_1]|_i +$$

$$+[(-W_n+v_n)\rho\Gamma_2]|_{j+1} - [(-W_n+v_n)\rho\Gamma_2]|_j\};$$

$$(\rho v_1)^{i+\frac{1}{2},j+\frac{1}{2}} = \frac{\sigma_{i+\frac{1}{2},j+\frac{1}{2}}}{\sigma^{i+\frac{1}{2},j+\frac{1}{2}}}(\rho v_1)_{i+\frac{1}{2},j+\frac{1}{2}} -$$

$$-\frac{\tau}{\sigma^{i+\frac{1}{2},j+\frac{1}{2}}}\{[(-W_n+v_n)\rho v_1 + P\cos\alpha_1]\Gamma_1|_{i+1} - [(-W_n+v_n)\rho v_1 + P\cos\alpha_1]\Gamma_1|_i +$$

$$+[(-W_n+v_n)\rho v_1 + P\cos\alpha_2]\Gamma_2|_{j+1} - [(-W_n+v_n)\rho v_1 + P\cos\alpha_2]\Gamma_2|_j\};$$

(38)

$$(\rho v_2)^{i+\frac{1}{2},j+\frac{1}{2}} = \frac{\sigma_{i+\frac{1}{2},j+\frac{1}{2}}}{\sigma^{i+\frac{1}{2},j+\frac{1}{2}}}(\rho v_2)_{i+\frac{1}{2},j+\frac{1}{2}} -$$

$$-\frac{\tau}{\sigma^{i+\frac{1}{2},j+\frac{1}{2}}}\{[(-W_n+v_n)\rho v_2 + P\cos\beta_1]\Gamma_1|_{i+1} - [(-W_n+v_n)\rho v_2 + P\cos\beta_1]\Gamma_1|_i +$$

$$+[(-W_n+v_n)\rho v_2 + P\cos\beta_2]\Gamma_2|_{j+1} - [(-W_n+v_n)\rho v_2 + P\cos\beta_2]\Gamma_2|_j\};$$

$$\rho\left(\frac{1}{k-1}\frac{P}{\rho}+\frac{v_1^2+v_2^2}{2}\right)^{i+\frac{1}{2},j+\frac{1}{2}}=\frac{\sigma_{i+\frac{1}{2},j+\frac{1}{2}}}{\sigma^{i+\frac{1}{2},j+\frac{1}{2}}}\rho\left(\frac{1}{k-1}\frac{P}{\rho}+\frac{v_1^2+v_2^2}{2}\right)_{i+\frac{1}{2},j+\frac{1}{2}}-$$

$$-\frac{\tau}{\sigma^{i+\frac{1}{2},j+\frac{1}{2}}}\{[\rho\left(\frac{1}{k-1}\frac{P}{\rho}+\frac{v_1^2+v_2^2}{2}\right)(-W_n+v_n)+Pv_n]\Gamma_1|_{i+1}-$$

$$-[\rho\left(\frac{1}{k-1}\frac{P}{\rho}+\frac{v_1^2+v_2^2}{2}\right)(-W_n+v_n)+Pv_n]\Gamma_1|_i+$$

$$+[\rho\left(\frac{1}{k-1}\frac{P}{\rho}+\frac{v_1^2+v_2^2}{2}\right)(-W_n+v_n)+Pv_n]\Gamma_2|_{j+1}-$$

$$-[\rho\left(\frac{1}{k-1}\frac{P}{\rho}+\frac{v_1^2+v_2^2}{2}\right)(-W_n+v_n)+Pv_n]\Gamma_2|_j\}.$$

The calculated formulas (38) represented the conservation laws, written in the discrete form for any grid cell and defined the change of density, momentum and the energy versus mass, impulse and energy fluxes through the cell surfaces.

Gasdynamic parameters on lateral sides (expressions in square brackets), obtained from the solution of the local Riemann problem at the cell interfaces, must be found. This is the physical step of the whole procedure. The discontinuities at the interfaces are resolved in a superposition of waves satysfying locally the conservations equations. (see Godunov [11], p. 105, 130, Hirsch [15], p. 443, Chmielniak [9], p. 160).

Time step τ is constant for all calculated domain and is calculated from the stability condition of the explicit scheme.

$$\tau < \tau_1\tau_2/(\tau_1+\tau_2), \tag{39}$$

$$\tau_1 = h_1/\max(a_0+v_1, a_0-v_1), \tag{40}$$

$$\tau_2 = h_2/\max(a_0+v_2, a_0-v_2), \tag{41}$$

where h_1, h_2 are the steps of the difference scheme in x and y directions, a_0 the sound velocity, v_1, v_2 the velocities components in x and y directions.

3.1 The Kolgan modification

One of the most important assumptions in the difference schemes is the possibility of accurate calculation in the nonorthogonal and nonregular schemes, with cells of different size. In the Godunov scheme the distribution of the parameters in the cells is uniform, so it is the discontinuities between adjacent cells. In the boundary of the cells we take the parameters from the adjacent cells. In the Godunov–Kolgan scheme the parameters in the boundary of the cells depend linearly on the parameters of the adjacent cells.

Let's assume that :

f_0 is the value in the center of 0 cell (see Figure 7);
f_1 is the value in the center of 1 cell;
f_2 is the value in the center of 2 cell;
f_3 is the value in the center of 3 cell;
f_4 is the value in the center of 4 cell;
y_0, x_0 are coordinates of the center of 0 cell;
y_1, x_1 are coordinates of the center of 1 cell;
y_2, x_2 are coordinates of the center of 2 cell;
y_3, x_3 are coordinates of the center of 3 cell;
y_4, x_4 are coordinates of the center of 4 cell;
$dy_1 = y_1 - y_0$;
$dx_1 = x_1 - x_0$;
$dy_2 = y_2 - y_0$;
$dx_2 = x_2 - x_0$;
$dy_3 = y_3 - y_0$;
$dx_3 = x_3 - x_0$;
$dy_4 = y_4 - y_0$;
$dx_4 = x_4 - x_0$.

The values of $\frac{\partial f}{\partial x}$ and $\frac{\partial f}{\partial y}$ are found from the assumption of Kolgan of the minimum of the derivatives.

One set of $\left(\frac{\partial f}{\partial x}\right)_1$ and $\left(\frac{\partial f}{\partial y}\right)_1$ can be found from equations for zero, one and two cells:

$$\begin{aligned} f_1 &= f_0 + \left(\frac{\partial f}{\partial x}\right)_1 dx_1 + \left(\frac{\partial f_0}{\partial y}\right)_1 dy_1, \\ f_2 &= f_0 + \left(\frac{\partial f_0}{\partial x}\right)_1 dx_2 + \left(\frac{\partial f_0}{\partial y}\right)_1 dy_2. \end{aligned} \tag{42}$$

From the above equation we can find in the unique way the $\left(\frac{\partial f}{\partial x}\right)_1$ and $\left(\frac{\partial f}{\partial y}\right)_1$, when the lines connecting the zero to the first, and the zero to the second cell, are not in line.

In a similar way we can find $\left(\frac{\partial f}{\partial x}\right)_2$ and $\left(\frac{\partial f}{\partial y}\right)_2$ for the third and fourth cells:

$$\begin{aligned} f_3 &= f_0 + \left(\frac{\partial f_0}{\partial x}\right)_2 dx_3 + \left(\frac{\partial f_0}{\partial y}\right)_2 dy_3, \\ f_4 &= f_0 + \left(\frac{\partial f_0}{\partial x}\right)_2 dx_4 + \left(\frac{\partial f_0}{\partial y}\right)_2 dy_4. \end{aligned} \tag{43}$$

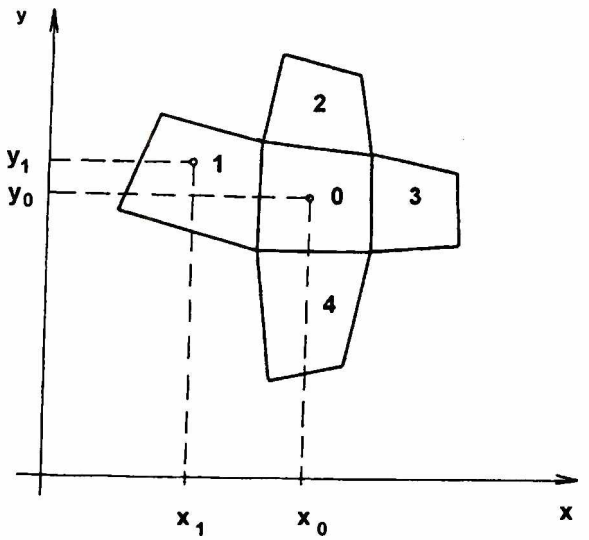

Figure 7. *The Kolgan approximation*

So, the values $\left(\frac{\partial f}{\partial x}\right)$ and $\left(\frac{\partial f}{\partial y}\right)$ for approximation of parameter in the zero cells can be found:

$$\left(\frac{\partial f_0}{\partial x}\right) = \min\left(abs\left(\frac{\partial f}{\partial x}\right)_1, abs\left(\frac{\partial f}{\partial x}\right)_2\right) sign\left[\left(\frac{\partial f_0}{\partial x}\right)_1\right]$$

for

$$\left(\frac{\partial f}{\partial x}\right)_1 \cdot \left(\frac{\partial f}{\partial x}\right)_2 > 0$$

and

$$\left(\frac{\partial f}{\partial x}\right) = 0$$

for

$$\left(\frac{\partial f}{\partial x}\right)_1 \cdot \left(\frac{\partial f}{\partial x}\right)_2 \le 0.$$

Similarly

$$\left(\frac{\partial f_0}{\partial y}\right) = \min\left(abs\left(\frac{\partial f}{\partial y}\right)_1, abs\left(\frac{\partial f}{\partial y}\right)_2\right) sign\left[\left(\frac{\partial f_0}{\partial y}\right)_1\right]$$

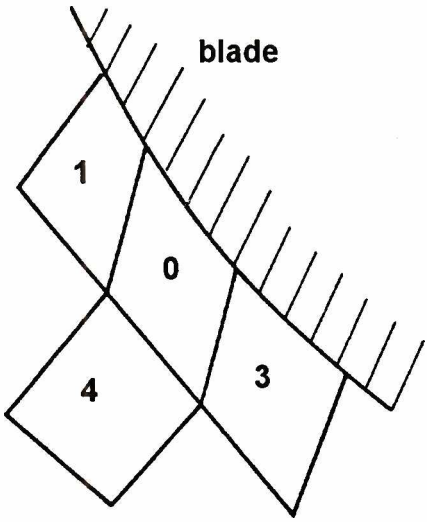

Figure 8. *The Kolgan approximation close to the blade*

for

$$\left(\frac{\partial f}{\partial y}\right)_1 \cdot \left(\frac{\partial f}{\partial y}\right)_2 > 0,$$

and

$$\left(\frac{\partial f}{\partial y}\right) = 0$$

for

$$\left(\frac{\partial f}{\partial y}\right)_1 \cdot \left(\frac{\partial f}{\partial y}\right)_2 \le 0. \tag{44}$$

The above values are used to calculate gasodynamic parameters in the centre of cell boundary, which are used in the discontinuity between adjacent cells. The Godunov–Kolgan scheme, described above, is monotonous, there is a small difference between densities in the adjacent cells and the tangential discountinity. The scheme presented above is of the second aproximation order in the x and y variable and is the first order approximation of time. The way of estimation of the derivatives of f according to conditions (44) gives possibilities to get positive values of pressure and density as results of linear approximation:

$$f_g = f_0 + \left(\frac{\partial f}{\partial x}\right)(x_g - x_0) + \left(\frac{\partial f}{\partial y}\right)(y_g - y_0), \tag{45}$$

where f_g is the value on the boundary of the cell; y_g, x_g are the coordinates of the center of the boundary of the cell.

In the case of nostationary flow the above consideration is not sufficient. The linear approximation must be written in the form:

$$f_g = f_0 + \left(\frac{\partial f}{\partial x}\right)(x_g - x_0) + \left(\frac{\partial f}{\partial y}\right)(y_g - y_0) + \left(\frac{\partial f}{\partial t}\right)(t - t_0), \tag{46}$$

where t_0 is the time of the past time iteration. For the derivatives in time, differential equations (26) were written in the form:

$$\begin{aligned}
\frac{\partial \rho}{\partial t} &= -\left[\rho\left(\frac{\partial v_1}{\partial x} + \frac{\partial v_2}{\partial y}\right) + v_1\frac{\partial \rho}{\partial x} + v_2\frac{\partial \rho}{\partial y}\right],\\
\frac{\partial v_1}{\partial t} &= -\left[\frac{1}{\rho}\frac{\partial p}{\partial x} + v_1\frac{v_1}{\partial x} + v_2\frac{v_1}{\partial y}\right],\\
\frac{\partial v_2}{\partial t} &= -\left[\frac{1}{\rho}\frac{\partial p}{\partial y} + v_1\frac{v_2}{\partial x} + v_2\frac{v_2}{\partial y}\right],\\
\frac{\partial p}{\partial t} &= -\left[p\left(\frac{\partial v_1}{\partial x} + \frac{\partial v_2}{\partial y}\right) + v_1\frac{\partial p}{\partial x} + v_2\frac{\partial p}{\partial y}\right].
\end{aligned} \tag{47}$$

From equation (46) the parameters of the flow are calculated in the centre of boundary cells for the time $t_0 = t_0 + \delta t/2$. Such modification allows t_0 increase the step calculation time twice in comparison to the Godunov–Kolgan scheme and the total time of calculation is decreased by 40 %. That scheme is of second aproximation order in the x and y variable and is of the second order approximation of time and is monotonous.

3.2 The boundary conditions

The boundary conditions formulation is based on one–dimensional theory of the characteristics. According to this theory some gasdynamic parameters on the boundary of calculated domain, in the unsteady flow, characterize the influence of the external domain (these parameters are imposed as the boundary conditions) and some parameters characterize perturbation coming from the internal domain (these ones are defined from characteristic relations).

The number of boundary conditions depends on the flow conditions. When axial velocity is subsonic, the following boundary conditions are imposed. At the inlet of calculated domain — the total temperature T_0, the total pressure P_0, and the entropy:

$$\frac{P_0}{R_0^k} = \frac{P}{R^k},$$

the flow angle β_1:

$$\frac{V_2}{V_1} = \tan\beta_1,$$

the entalphy:

$$\frac{k}{k-1}\frac{P_0}{\rho_0}=\frac{k}{k-1}\frac{P}{R}+\frac{V_1^2+V_2^2}{2}, \tag{48}$$

and the left Riemann invariant:

$$v_1-\frac{2}{k-1}\sqrt{k\frac{p}{\rho}}=V_1-\frac{2}{k-1}\sqrt{k\frac{P}{R}},$$

at the exit for the subsonic flow– the static pressure P_2, the right Riemann invariant:

$$V_1+\frac{2}{k-1}\sqrt{k\frac{p}{\rho}}=const.$$

the isentrophy condition, when the pressure in the boundary cells is greater than the inflow pressure or the adiabate Hugoniot, when the pressure in the boundary cells is lower than the static outflow pressure. The condition of equality of tangential velocity components in the output cross–section and close to the left side of the cells.

In the case of the supersonic inflow the velocity components V_1, V_2 must be assumed. If the outflow is supersonic, the continuation condition is applied to all parameters at the downstream boundary.

The solid–wall boundary condition appropriate for inviscid flow computations is that of zero mass flux through the surface. This condition is difficult to implement uniquely for the Euler equation. In this case the effect of the shock reflection was used [5].

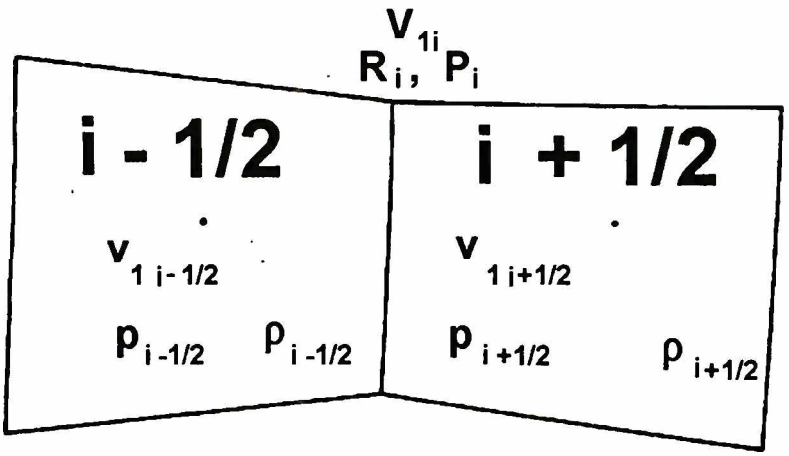

Figure 9. The small and big values of the cell in x direction

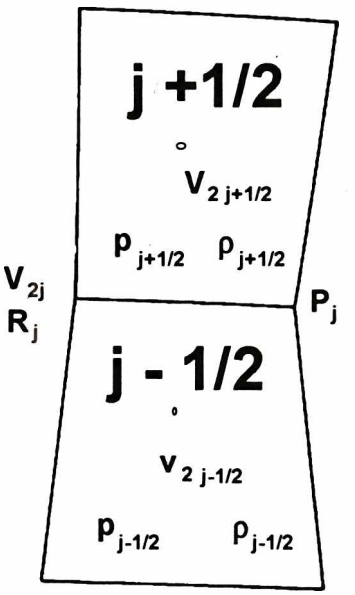

Figure 10. *The small and big values of the cell in y direction*

4. Integration of coupled aeroelastic system

In the case of aeroelastic problem the unknown gasdynamic parameters depend on both the position and velocity of the oscillating blades (so the moving grids were used). At the same time the blade motion depends on the instant aerodynamic load. In the literature the flutter problem was analysed by assumption of the specified movement of the blade (the interblade phase angle) so the fluid–structure problem was coupled from one side.

In this work we are going to present the partially–integrated method to solve the coupled fluid–structure problem.

Therefore the natural way of solving the aeroelastic problem is simultaneous integration of the full coupled set of aerodynamics equations (26) and the structure equations (25) or (4). The numerical digitization can be realized by way of the parallel solving of two equations (26, 25) or (26, 4) during every time step under the same initial data without any priority of both problems. As initial data for both problems, the instant aerodynamic loads, velocity and position of every blade, obtained from the coupled system on previous time step, was assumed. The common time step is limited by the stability condition of the aerodynamic problem.

5. The numerical results

The numerical test calculations were performed to compare theoretical results obtained by use of the mathematical model developed here, and the experimental results presented by Bölc and Fransson [8]. The calculations were carried out for the torsion oscillations of the compressor blades (The First Standard Configuration) and the bending oscillations of the turbine blades (The Fourth Standard Configuration).

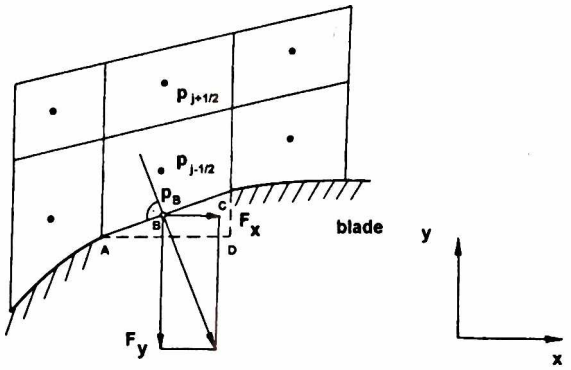

Figure 11. The forces acting on the blade

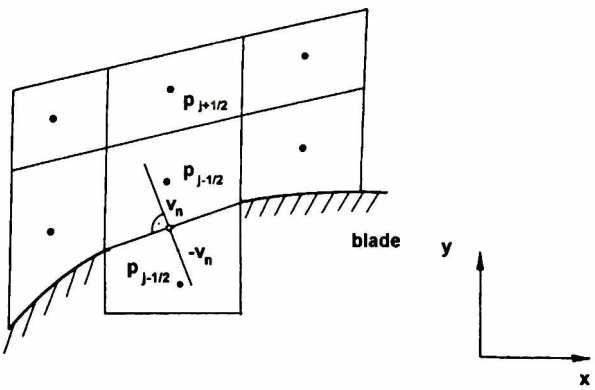

Figure 12. The boundary condition on the blade

5.1 Torsional oscillations. The First Standard Configuration

The cascade configuration (The First Standard Configuration (see Figure 13)) being investigated, consists of eleven vibrating blades, each having a chord $c = 0.1524$ m and a span of 0.254 m, with a 10° circular arc chamber and a thickness–to–chord ratio of 0.06.

The pitch–to–chord ratio is 0.75 and the stagger angle is 55°. The experiments were performed in the air. In the calculations, an ideal gas was accepted as working medium.

The flow regime was determined:

— at the inlet the total temperature and the total pressure are equal to 315° K and 10^5 Pa respectively, the incidence angle is $i = 6°$;

— at the exit static pressure was held up to $0.98520 \cdot 10^5$ Pa.

The calculation of the flow through cascade of blades, vibrating with frequency $f = 15.5$ Hz and pitching amplitude $\alpha = 2°$ for different phase angles between adjacent blades motion were performed. The positive angle corresponds to the direction opposite to the rotation (see Figure 2).

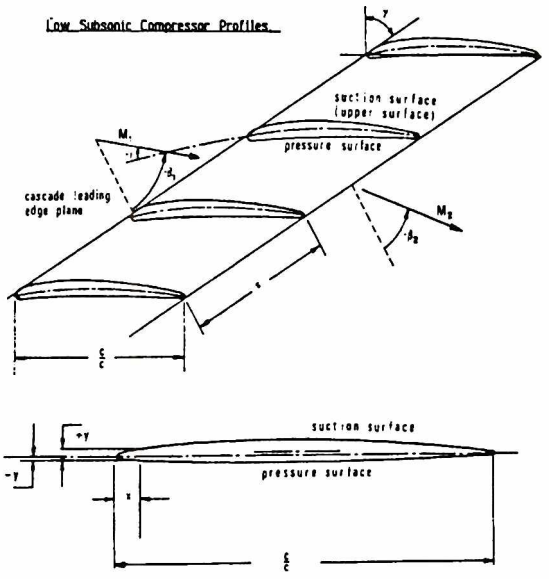

***Figure 13.** First Standard Configuration*

The Fourier analysis was used for calculated numerical results:

$$C(t) = C_0 + \sum_{n=1}^{\infty}(C_n^a \cos n\omega t + C_n^b \sin n\omega t) = C_0 + \sum_{n=1}^{\infty}(C_n^{ab} \cos(n\omega t + \varphi_n)), \quad (49)$$

where $C(t)$ is the physical value being investigated; φ_n is the phase of the n–th harmonic; C_0, C_n^a, C_n^b, C_n^{ab} (n = 1, 2, 3, ...) are Fourier coefficients. At the steady regime all flow parameters are changed by the harmonic law with period $T = 2\pi/\omega = 1/f$.

The validity of theoretical results can be established only by agreement between the measured and calculated pressure distribution on both blade surfaces. The comparisons of time averaged pressure coefficients and Mach number distributions along the blade chord were shown in Figures 14 and 15.

The pressure coefficient is defined:

$$C_p(x) = \frac{P(x) - P_1}{P_0 - P_1}, \quad (50)$$

where P_0 is total pressure, P_1 and $P(x)$ are the time averaged static pressure at the inlet, and the local static pressure at the point x of the chord, respectively.

Apart from the discrepancies near the leading edge, caused by the different definition of the incidence angle in the experiment and calculation (this discrepancy is about 2.5°), agreement with experiment is quite good.

The stability of system "flow–cascade" without taking into account the material damping, is defined by aerodynamic work coefficient Ψ, performed by the aero-

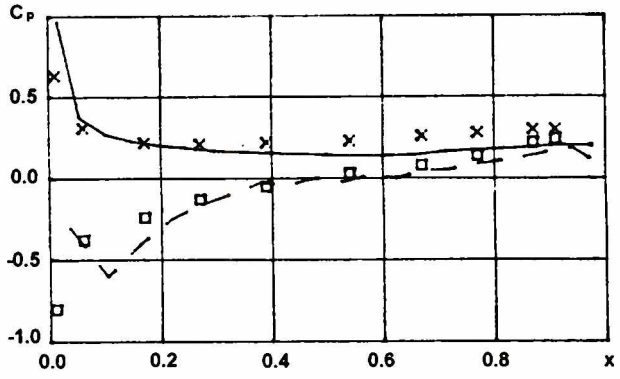

Figure 14. First Standard Configuration. M1 = 0.17. f = 15.5 Hz. Time averaged blade surface pressure distribution. ——— Pressure side calculation. — — — Suction side calculation. × × × Pressure side experiment. □□□ Suction side experiment

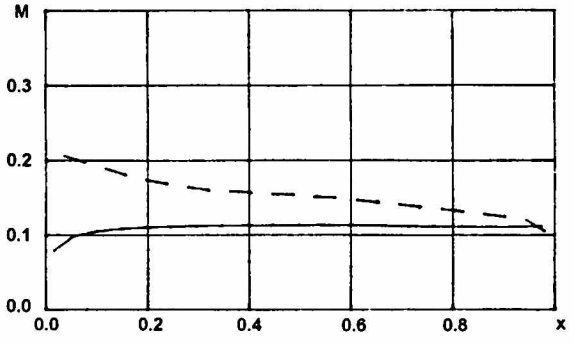

Figure 15. First Standard Configuration. M1 = 0.17. f = 15.5 Hz. Isentropic Mach number distribution. ——— Pressure side calculation. — — — Suction side calculation

dynamic forces during one cycle of oscillating. In Figure 16 the aerodynamic work coefficient:

$$\Psi = \frac{W}{(P_0 - P_1) b^3 \pi A^2}, \tag{51}$$

versus the interblade phase angle δ is presented. Here $A = \alpha$ for the torsion vibrations, and $A = h/h_0$ for the bending vibrations. The positive values of Ψ correspond to the transfer energy from the flow to the blade ("negative" aerodamping, or self–excitation), whereas the negative values — to the dissipation of blade energy to the flow ("positive" aerodamping). As it is seen from Figure 16, some scattering appears in the magnitude of the work coefficient around its maximum and minimum values (near +90° and +90° interblade phase angle). Generally, the theoretical and experimental results agreed well. The maximum negative and positive values under $\delta = -90°$, and $\delta = -90°$, correspond to maximum values of the damping coefficient, and the excitation coefficient (flutter), respectively.

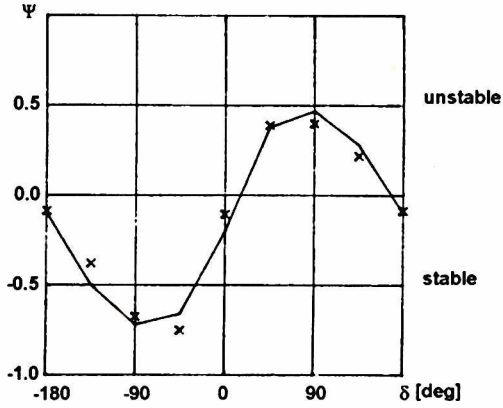

Figure 16. First Standard Configuration. M1 = 0.17. f = 15.5 Hz. Aerodynamic work coefficient versus interblade phase angle. ———— Calculation. ××× Experiment

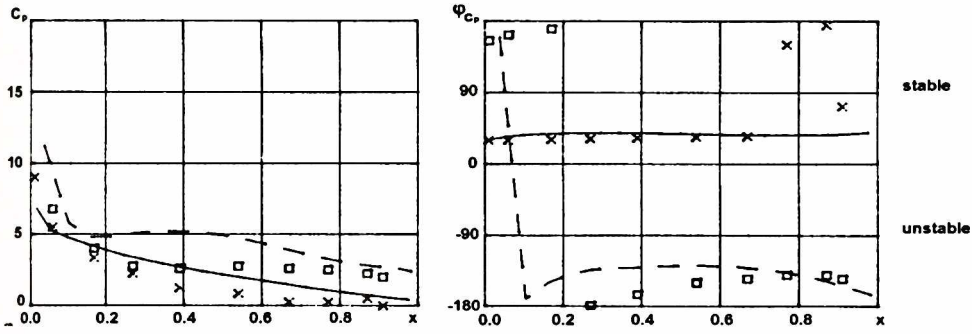

Figure 17. First Standard Configuration. M1 = 0.17. f = 15.5 Hz. Magnitude and phase of unsteady blade surface pressure coefficient. δ = –90°. ———— Pressure side calculation. — — — Suction side calculation. × × × Pressure side experiment. □ □ □ Suction side experiment

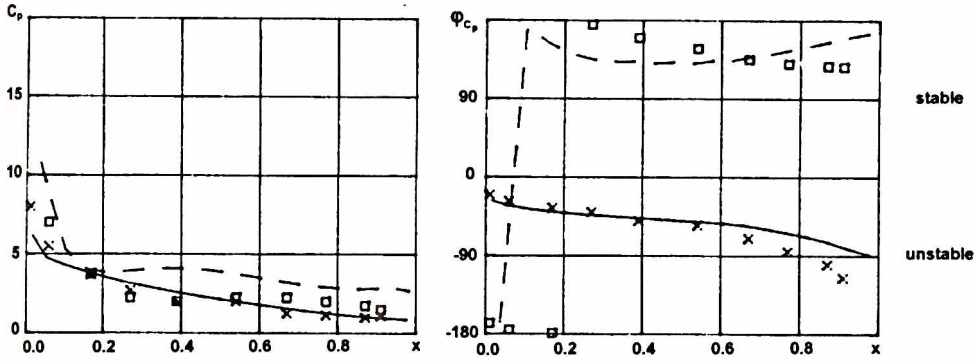

Figure 18. First Standard Configuration. M1 = 0.17. f = 15.5 Hz. Magnitude and phase of unsteady blade surface pressure coefficient. δ = 90°. ———— Pressure side calculation. – – – Suction side calculation. × × × Pressure side experiment. □□□ Suction side experiment

The first harmonic amplitude and the phase of the unsteady pressure coefficient:

$$\tilde{C}_p(x) = \frac{\tilde{P}(x)}{(P_0 - P_1)A} \tag{52}$$

along the blade chord for interblade phase angles $\delta = -90°, +90°$ was shown in Figures 17 and 18. Here $\tilde{P}(x)$ is the unsteady pressure at the x–point of the blade chord. From those diagrams it is seen that the phase angles on the suction blade surfaces are better predicted than the pressure amplitudes. The largest difference between experimental and numerical results is observed on the suction side in the middle of the blade. Figure 19 presents the unsteady aerodynamic moment coefficient:

$$\tilde{C}_m(t) = \frac{\tilde{M}(t)}{(P_0 - P_1)b^3\pi A}, \tag{53}$$

and its phase angle with respect to the blade motion versus the interblade phase angle. Here $\tilde{M}(x)$ is the unsteady moment at the x–point of the blade chord. From these diagrams it can be seen that the blade behavior (flutter or damping) does not depend on the aerodynamic moment value, but on the phase angle shift of the unsteady moment with respect to the blade motion. In the assumption of zero material damping, the positive phase angles correspond to the selfexcitation (flutter), the negative — to the aerodynamic damping.

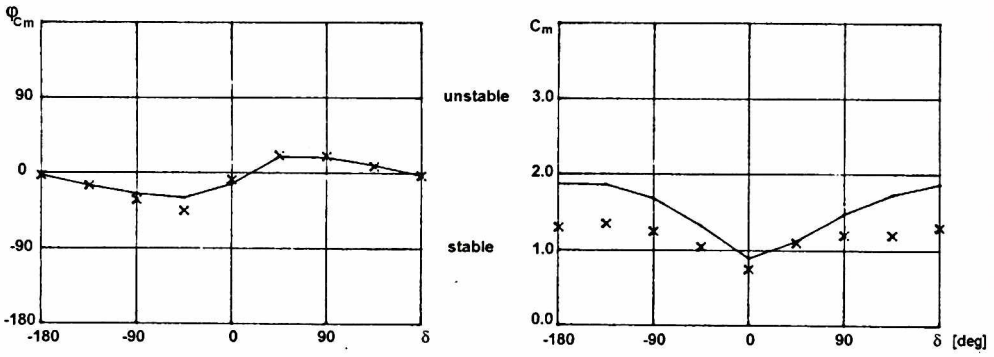

Figure 19. *First Standard Configuration. M1 = 0.17. f = 15.5 Hz. Aerodynamic moment coefficient and phase in dependence of interblade phase angle. ———— Calculation. ××× Experiment*

The correspondence between the aerodynamic moment and the blade motion (the torsion angle for the mean position) is presented in Figure 20. In this Figure the hysteresis phenomenon (the moment depends not only on the motion angle, but on the motion direction) is observed. In addition, in Figure 20 the changing of the moment direction under the blade motion in the positive direction is denoted by an arrow. The area of hysteresis loop is equal to the aerodynamic work during one cycle of the oscillation, and the work sign is determined by the loop direction, pointed out with the arrow. For the phase angles $\delta = 45°, 90°, 135°$ the aerodynamic work coefficient is positive, so the self–excited oscillations occur (see Figure 20). For the

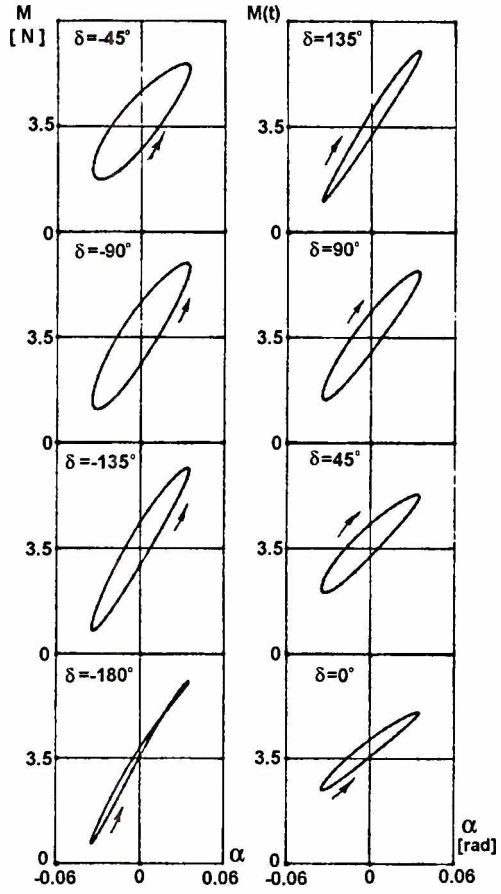

Figure 20. *First Standard Configuration. M1 = 0.17. f = 15.5 Hz. Aerodynamic moment versus torsion angle*

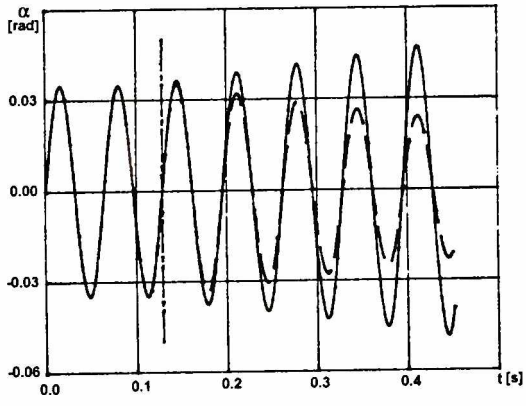

Figure 21. *First Standard Configuration. M1 = 0.17. f = 15.5 Hz. Torsion angle for flutter and aerodamping regimes. ———— Flutter. — — — Damping. — · — · — Up this line the kinematic excitation without the aerodynamic force exists*

phase angle $\delta = -180°, -135°, -90°, -45°, 0°$ the aerodynamic damping occurs. The loop distortion is connected with nonlinearity between the moment and the blade motion. In case of the low work coefficient, the hysteresis loop can be deformed like the digit 8 (see Figure 20, $\delta = -180°$). This means that the sign of the aerodynamic work is changing for the considered phase angle.

Next, the calculations were performed on the basis of joint solving of the coupled set of equations (26) and two degrees of freedom blade model (the material damping was neglected).

The blades positions and velocities, obtained from the kinematic calculation were accepted as the initial data of the coupled problem. Figure 21 shows the blade motion for the initial interblade phase angles $\delta = +90°$ (flutter, solid line) and $\delta = -90°$ (damping, dashed line). In both cases an increase of the period of the oscillation was observed. This can be explained by the existence of the aerodamping. The similar results were obtained using the continues blade model.

5.2 Oscillations in bending mode. The Fourth Standard Configuration

The investigations of bending oscillations of the high load turbine rotor sections were performed for the Fourth Standard Configuration (see Figure 22). This type of airfoil has a relatively high blade thickness and camber and operates under high subsonic flow conditions.

The cascade configuration consists of 20 vibrating prismatic blades, each with a chord of $c = 0.0744$ m with 45° turning and a maximum thickness–to–chord ratio of 0.17.

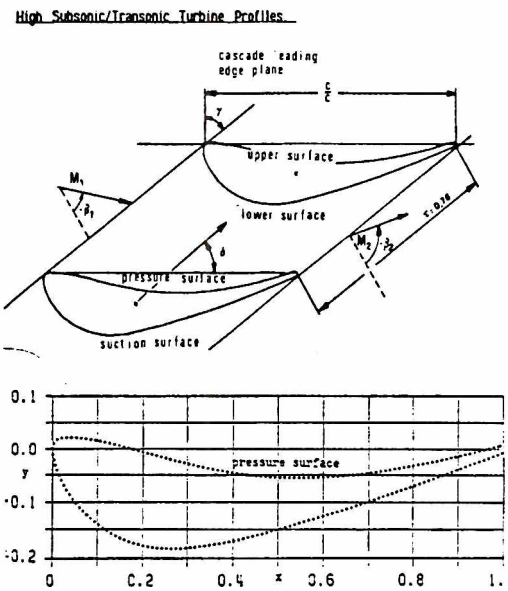

Figure 22. Fourth Standard Configuration

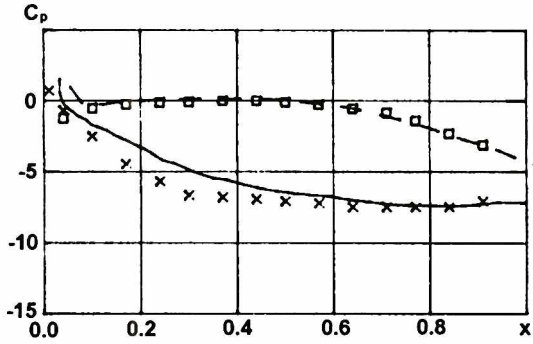

Figure 23. *Fourth Standard Configuration. M2 = 0.9. f = 150 Hz. Time averaged blade surface pressure distribution. ——— Suction side calculation. — — — Pressure side calculation. ××× Suction side experiment. □□□ Pressure side experiment*

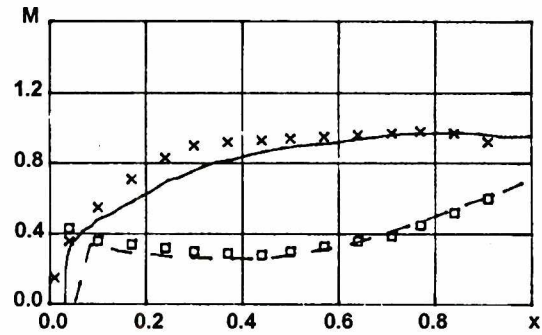

Figure 24. *Fourth Standard Configuration. M2 = 0.9. f = 150 Hz. Isentropic Mach number distribution. ——— Suction side calculation. — — — Pressure side calculation. ××× Suction side experiment. □□□ Pressure side experiment*

The stagger angle is 56.6° with the pitch–to–chord ratio of the cascade:
0.67 (hub)
0.76 (midspan)
0.84 (tip)

The hub–tip ratio in the test is 0.8. The calculations were performed under inlet flow velocity $M_1 = 0.28$, expansion ratio $\varepsilon = P_2 / P_0 = 0.589$ ($P_0 = 2.058 \cdot 10^6$ Pa, $P_2 = 1.212 \cdot 10^6$ Pa, $M2 = 0.9$); oscillating frequency $f = 150$Hz; the inlet flow angle $\beta_1 = -45°$ and different interblade phase angles.

The time averaged surface pressure coefficient, and the isentropic Mach number distributions along the blade chord in Figures 23 and 24, respectively are presented. The agreement between the calculated and the experimental results is good.

In Figure 25 the aerodynamic work coefficient is presented as a function of the interblade phase angle for inlet flow angle, and equals – 45°. The sinusoidal shape, similar to the first configuration, is recognized, although the unstable region is smaller

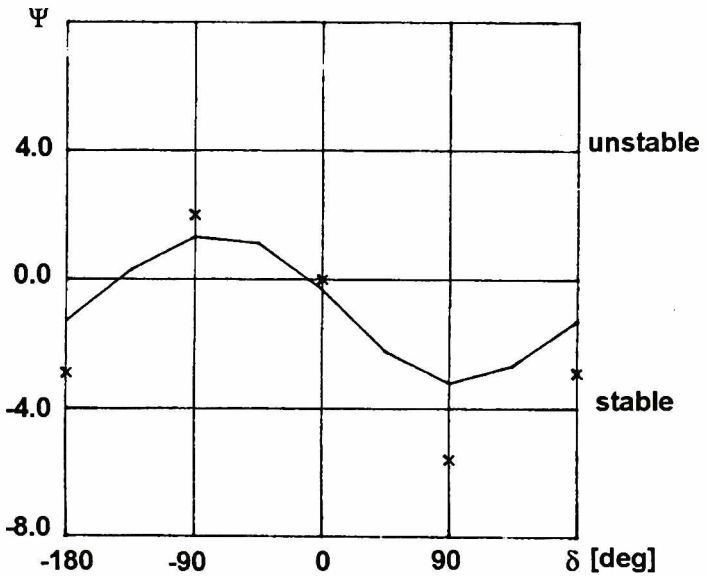

Figure 25. Fourth Standard Configuration. M2 = 0.9. f = 150 Hz. Aerodynamic work coefficient in dependence of interblade phase angle. ———— Calculation. ××× Experiment

than the stable region. As it has been seen from Figure 25, the cascade shows instability in subsonic flow for the interblade phase angle around $\delta = -90°$. The shape of aerodynamic work coefficient versus the interblade phase angle is similar for both the theory and the experiment. However, the maximal and minimal numerical values of damping are smaller than the measured ones. The reason for the discrepancy between the experiment and theory is found by examining the local pressure coefficient distribution along the blade chord (see Figure 26 and 27). It is seen, that the theory predicts a somewhat smaller pressure value along the whole suction surface than the experiment for the same interblade phase angles. However, it is difficult to explain why the difference between experiment and theory occurs.

The change of the aerodynamic force as a function of a blade motion is shown in Figure 28. The positive values of the work coefficient for the interblade phase angle $\delta = -135°, -90°, -45°$ correspond to the flow instability. In that case the hysteresis character of this dependence is similar to results presented for the First Standard Configuration (Figure 20).

Figure 29 presents the blade motion, obtained from solving the coupled aeroelastic problem for two interblade phase angles: at $\delta = -90°$ (flutter, solid line) and $\delta = +90°$ (damping, dashed line) using the two degree of freedom blade model.

Using the continues model for all blade interblade phase angles the flutter conditions were not found.

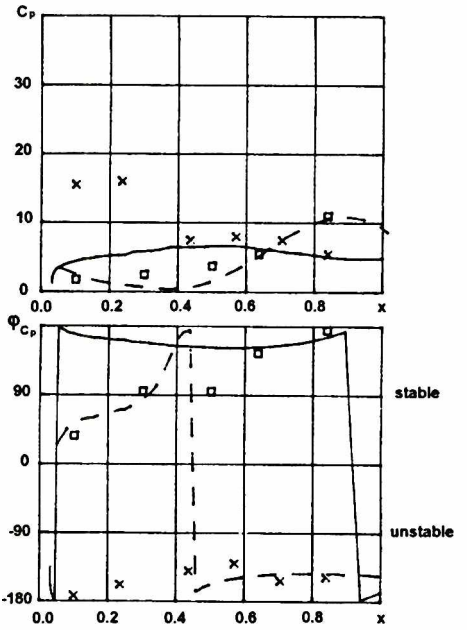

Figure 26. *Fourth Standard Configuration. M2 = 0.9. f = 150 Hz. Magnitude and phase of unsteady blade surface pressure coefficient. δ = -90°. ———— Suction side calculation. — — — Pressure side calculation. × × × Suction side experiment. □□□ Pressure side experiment*

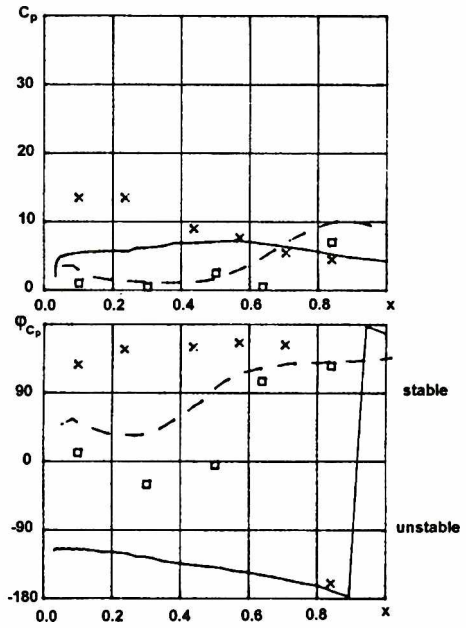

Figure 27. *Fourth Standard Configuration. M2 = 0.9. f = 150 Hz. Magnitude and phase of unsteady blade surface pressure coefficient. δ = 90°. ———— Suction side calculation. — — — Pressure side calculation. × × × Suction side experiment. □□□ Pressure side experiment*

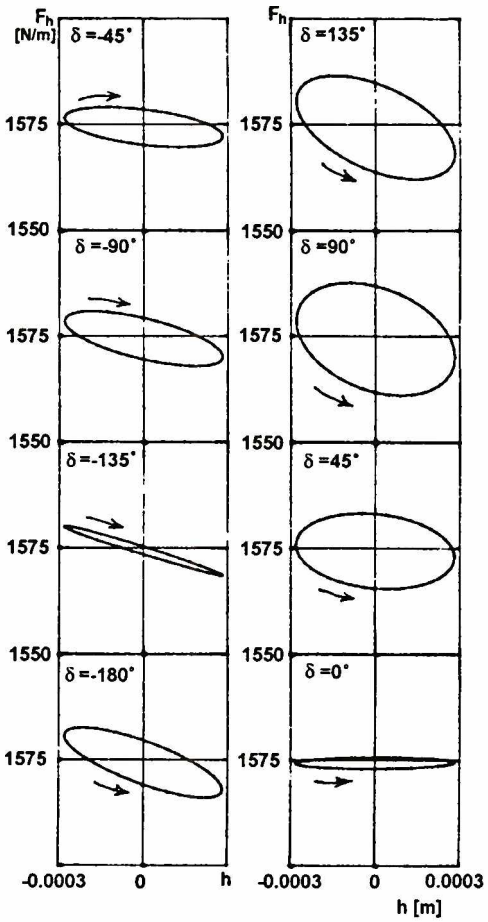

Figure 28. *Fourth Standard Configuration. M2 = 0.9. f = 150 Hz. Aerodynamic force versus bending movement*

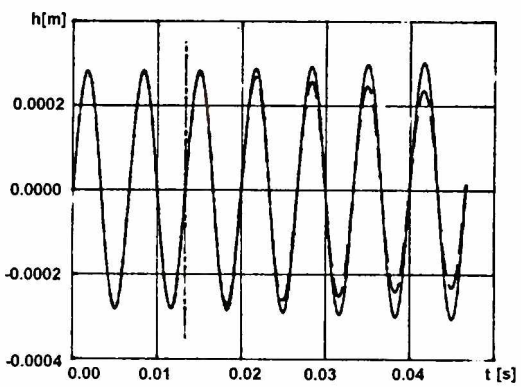

Figure 29. *Fourth Standard Configuration. M2 = 0.9. f = 150 Hz. Bending movement for flutter and aerodamping regimes. ———— Flutter. — — — Damping. — · — · —. Up this line the kinematic excitation without the aerodynamic force exists*

6. Conclusions

— In this study the numerical method to predict the aeroelastic behavior of the compressor and the turbine cascades in two–dimensional transonic flow for shock–free flows is presented.

— The good agreement between the unsteady experimental and numerical results validates the possibility to predict the stability limits of the cascades (for zero material damping). The shapes of both theoretical and experimental damping curves are almost identical, but the magnitude shows small disagreement.

— In most cases the amplitudes and phase angles of the unsteady blade surface pressure coefficient are also predicted well. These values can be used to explain from which part of the blade the aerodynamic damping (excitation) appears.

All numerical calculations were made at the Academic Computer Center TASK (Gdansk, Poland).

References

[1] Agnew R.P., *Differential Equations*, Mcgraw–Hill Company, Inc., 1960

[2] Arkadyev A.B., Gnesin V.I., Vanin V.A. and Yershov S.V., *Unsteady Blade Forces Generated By Rotor–Stator Aerodynamic Interaction and Cascade Airfoils Oscillations*, International Conference Engineering Aerohydroelasticity EAHA, December 5–8, Prague, Czech Republic, 1989, 366

[3] Bakhale M.A., Reddy T.S.R. and Keith T.G., *Time Domain Flutter Analysis of Cascade Using Full–Potential Solver*, AIAA Journal, Vol. 30, No.1, January 1992, 163

[4] Bathe K. and Wilson E., *Numerical Methods in Finite Element Analysis*, Prentice–Hall, Inc., Englewood Cliffs, New Jersey, 1976

[5] Bendiksen O.O., *Role of Shock in Transonic/Supersonic Compressor Rotor Flutter*, AIAA Journal, Vol. 24, No. 7, July 1986, 1179

[6] Bisplinghoff R.L., Asley H. and Halfman R.L, *Aeroelasticity*, Addison–Wesley Publishing Company, Inc. Cambridge 42, Mass, 1955

[7] Bölsc A., and Fransson T.H., *Aeroelasticity in Turbomachines Comparison of Theoretical and Experimental Cascade Results*, Communication Du Laboratoire De Thermique Appliquée et Turbomachines, Nr.13. Lusanne, Epfel, 1986

[8] Bölsc A., and Fransson T.H., *Aeroelasticity in Turbomachines Comparison of Theoretical and Experimental Cascade Results*, Communication Du Laboratoire De Thermique Appliquée et Turbomachines, Nr.13, Appendix A5 All Experimental and Theoretical Results for The 9th Standard Configuration, Lusanne, Epfel, 1986

[9] Chmielniak T., *Foundation of The Theory of Profiles and Cascades*, Part IV Ossolineum Polish Academy of Sciences, The Institute of Flow–Fluid Machinery, 1989 (in Polish)

[10] Eidelman S, Colella P. and Shreeve R., *Application of The Godunov Method and Its Second–Order Extension To Cascade Flow Modeling*, AIAA Journal, vol. 22, No. 11, 1984, 1609

[11] Godunov, S.K. Et Al., *Numerical Solution of Multidimensional Problem in Gas Dynamics*, Nauka, Moscow, 1976 (in Russian)

[12] He L. and Denton J.D., *Three Dimensional Time–Marching Inviscid and Viscous Solutions For Unsteady Flows Around Vibrating Blades*, Asme Paper, 93–GT–92, 1993

[13] He L., *Rotating–Stall/Stall–Flutter Prediction Using A Fluid/Structure Coupled Method*, Proceedings of 7th International Symposium On Unsteady Aerodynamics and Aeroelasticity of Turbomachines, September 25–29, Fukuoka, Japan, 1994, 597

[14] Henry R. and Jacquet–Richardet G., *Flutter Analysis in Blade Dynamics*, 8th IFToMM World Congress, Theory of Machines and Mechanisms, Forced Vibrations of Turbomachine Blades, Prague, August 26–31, 1991

[15] Hirsch C., *Computation of Internal and External Flow*, vol. 2 Computational Methods For Inviscid and Viscous Flows, John Wiley and Son, 1988

[16] Ramamurti V., *Computer Aided Design in Mechanical Engineering*, Tata Mcgraw–Hill Publishing Company Limited, New Delhi, 1989

[17] Rozhdestvenskij B.L. and Yanenko N.N., *Systems of Quasilinear Equations and Their Applications To Gas Dynamics*, 2nd. Ed., Nauka, Moscow (1978), Engl. transl., Transl. Math Monographs, vol. 55, Providence (1983), Zbl.513.35002, Zbl.177,140

[18] Rządkowski R., *The General Model of Free Vibrations of Mistuned Bladed Discs.* Part I. *Theoretical Model.* Part II. *Numerical Results*, Journal of Sound and Vibration, 173(3), 1994, 395

[19] Rządkowski R., *Dynamics of Steam Turbine Rotor Blading*, Part II. *Bladed Discs*, Ossolineum, Wrocław, 1998

[20] Rządkowski R., *Numerical Analysis of Free and Forced Vibration of Tuned and Mistuned Bladed Discs*, Zeszyty Naukowe IMP PAN 483/1438/97 (PhD thesis)

[21] Rządkowski R., Gnesin V. and Kovalyov A., *The 2D Flutter of Bladed Disc in An In–Compressible Flow*, The 8th International Symposium of Unsteady Aerodynamics and Aeroelasticity of Turbomachines, Stockholm, Sweden, September 14–18 1997

[22] Verdon J.K., *Linearized Unsteady Aerodynamic Theory*, AGARD Manual On Aeroelasticity in Axial Flow Turbomachines, vol. 1, pp.(2–1, 2–31), 1987